Sequence and Context Dependence of EF-Hand Loop Dynamics. An ^{15}N Relaxation Study of a Calcium-Binding Site Mutant of Calbindin D_{9k}[†]

Anders Malmendal,* Göran Carlström, Charlotta Hambraeus, Torbjörn Drakenberg, Sture Forsén, and Mikael Akke

Physical Chemistry 2, Lund University, P.O. Box 124, S-221 00 Lund, Sweden

Received July 24, 1997; Revised Manuscript Received December 17, 1997

ABSTRACT: The influence of amino acid sequence and structural context on the backbone dynamics of EF-hand calcium-binding loops was investigated using ^{15}N spin relaxation measurements on the calcium-free state of the calbindin D_{9k} mutant (A14D+A15Δ+P20Δ+N21G+P43M), in which the N-terminal pseudo-EF-hand loop, characteristic of S100 proteins, was engineered so as to conform with the C-terminal consensus EF-hand loop. The results were compared to a previous study of the apo state of the wild-type-like P43G calbindin D_{9k} mutant. In the helical regions, the agreement with the P43G data is excellent, indicating that the structure and dynamics of the protein core are unaffected by the substitutions in the N-terminal loop. In the calcium-binding loops, the flexibility is drastically decreased compared to P43G, with the modified N-terminal loop showing a motional restriction comparable to that of the surrounding helixes. As in P43G, the motions in the C-terminal loop are less restricted than in the N-terminal loop. Differences in key hydrogen-bonding interactions correlate well with differences in dynamics and offer insights into the relationship between structure and dynamics of these EF-hand loops. It appears that the entire N-terminal EF-hand is built to form a rigid structure that allows calcium binding with only minor rearrangements and that the structural and dynamical properties of the entire EF-hand—rather than the loop sequence per se—is the major determinant of loop flexibility in this system.

The calcium ion is an important "second messenger" in a wide range of cellular processes, such as fertilization and muscle contraction (*1*−*3*). In many cases, the primary intracellular target is a protein with one or more pairs of cooperatively interacting helix−loop−helix calcium-binding motifs, commonly known as EF-hands (*4*). The ion-binding loops of EF-hand proteins exhibit a high degree of homology in sequence and structure (*5, 6*). The EF-hand family divides into distinct subfamilies, e.g., calmodulin, troponin C, parvalbumins, and S100 proteins (*7*). Some subfamilies, like the S100 proteins, are characterized by a loop architecture that deviates slightly from the consensus EF-hand (*8, 9*). EF-hand proteins with a regulatory function usually undergo large conformational changes upon calcium binding, enabling interactions with target proteins that trigger a cellular response, while those involved in ion buffering and transport respond to ion binding with only minor conformational changes.

Calbindin D_{9k} is a small (M_r 8500), monomeric calcium-binding protein of the S100 family, predominantly found in the epithelial cells of the small intestine and placenta, where it has been implicated in transcellular calcium transport (*10, 11*). Calbindin D_{9k} is the structurally best characterized EF-hand protein, with NMR solution structures available for the $(Ca^{2+})_2$, $(Cd^{2+})_1$, and ion-free (apo) states (*12*−*14*) and X-ray crystal structures for the $(Ca^{2+})_2$ and $(Mg^{2+})_1$ states (*15*−*17*). Calbindin D_{9k} consists of two helix−loop−helix EF-hand motifs that form a characteristic β-type interaction between the calcium-binding sites and are further connected by a linker segment at the opposite end of the molecule (Figure 1). The segments encompassing the residues involved in ion ligation are usually referred to as the calcium-binding loops, even though they start and end in the helixes flanking the actual loops. The N-terminal loop (loop I;[1] Figure 2A) has the pseudo-EF-hand sequence unique to the N-terminal EF-hands of the S100 proteins (*8, 9*), while the C-terminal calcium-binding loop (loop II; Figure 2B) conforms with the consensus regular EF-hand sequence (*4, 5*). The consensus loop II comprises 12 residues arranged to coordinate the calcium ion with pentagonal bipyramid

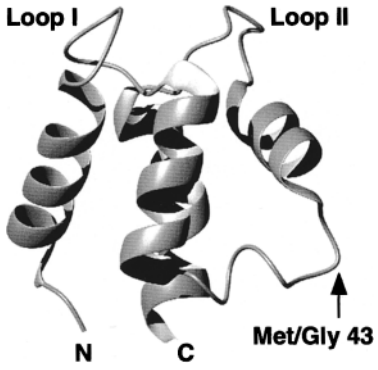

FIGURE 1: Ribbon diagram of calcium-loaded wild-type calbindin D_{9k}, PDB accession number 4icb (*16*) depicting the antipodal locations of the calcium binding loops and the linker in the structure. The distance between any atom in residue 43 and any of the backbone nitrogens in loops I and II that exhibit altered dynamics in 2EF is greater than 18 Å. The figure was generated using MOLMOL (*85*).

[†] This research was supported by Grant K-AA/KU 02545-326 from the Swedish Natural Science Research Council.

* Corresponding author: (fax) +46-46-222 4543; (e-mail) anders@bor.fkem2.lth.se.

S0006-2960(97)01798-4 CCC: $15.00
Published on Web 02/06/1998

FIGURE 2: Stereoimage of pseudo-EF-hand loop I (A) and regular EF-hand loop II (B) of calcium-loaded wild-type calbindin D_{9k}, PDB accession number 4icb (*16*). (A) The backbone atoms of residues 10−29 are shown in light gray, the side chains of the coordinating residues Ala14, Glu17, Asp19, and Gln22 are shown in dark gray, and the side chain of Glu27 is shown in black. (B) The backbone atoms of residues 50−67 are shown in light gray, the side chains of the coordinating residues Asp54, Asn56, Asp58, and Glu60 are shown in dark gray, and the side chain of Glu65 and the amide proton of Gly59 are shown in black. The dotted line indicates the Gly59 HN−Asp54 O^{δ} hydrogen bond. The figure was generated using UCSF software MidasPlus (*86*).

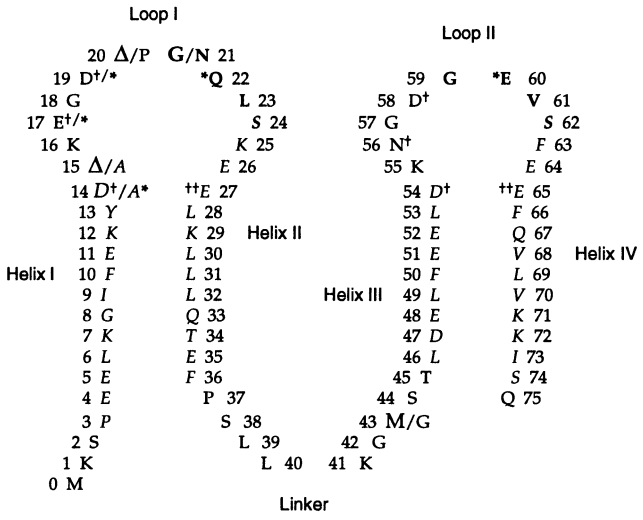

FIGURE 3: Amino acid sequence and secondary structure of 2EF and P43G calbindin D_{9k}. The one letter code is used for amino acid residues. The apo-P43G secondary structure (*13*) is indicated with α-helical residues in italic and *β*-sheet residues in boldface. Residues coordinating calcium with main-chain carbonyl oxygens are marked with an asterisk (*) and those using side-chain carboxylates with a dagger (†). In positions with amino acid substitutions, the residue type is indicated first for 2EF and second for P43G, e.g., (2EF/P43G).

symmetry, in which the seven ligands are provided by five side-chain carboxylate oxygens, one backbone carbonyl oxygen, and one water oxygen (*15, 16*). The coordinating residue in the first position of the loop is an invariant Asp (54),[2] and the residue in the twelfth and last position is a conserved bidentate Glu (65) (Figure 3). In the large majority of regular EF-hands, the sixth residue of the loop is a Gly (59), allowing the loop to make a 90° change in direction (*5*). In the calcium-bound state, regular EF-hands have a strong, stabilizing hydrogen bond between the amide proton of this Gly (59) and the nonligating carboxylate oxygen of Asp (54) in the first position (Figure 2B). The pseudo-EF-hand has a 14-residue-long loop that also coordinates calcium with pentagonal bipyramid symmetry, but the ligands are mainly backbone carbonyl oxygens, with the only exceptions being a bidentate carboxyl group of Glu (27) in the last position and a water oxygen (Figure 3) (*15, 16*). As a consequence of the different coordination pattern, the pseudo-EF-hand looks like a regular EF-hand loop turned inside-out, with its side chains oriented away from the location of the ion and toward the solvent (Figure 2A). In this site, the residue in the first coordinating position is an Ala (14) instead of an Asp, and there is no Gly in the sixth position (Figure 3). The N-terminal pseudo-EF-hand of calbindin D_{9k} is considerably more selective for calcium than the C-terminal regular EF-hand (*17, 18*).

Wild-type bovine calbindin D_{9k} exhibits cis−trans isomerization around the Gly42−Pro43 peptide bond in the flexible linker between the two EF-hands, resulting in two sets of resonances in the NMR spectrum (*19*). To circumvent this complication, the original structural and dynamical studies were made on the conformationally homogeneous P43G mutant (*20*). Subsequently, the P43M mutant was introduced to allow CNBr cleavage of the protein into its two EF-hand domains (Figures 1 and 3). Comparisons of chemical shifts of the P43G and P43M calbindin D_{9k} mutants showed that the chemical shift differences are highly localized to the site of mutation (*21, 22*); a direct comparison for the calcium-free states of P43G, P43M and 2EF is provided in Figure 4. Amide proton chemical shifts typically exhibit a larger degree of scatter than α-proton chemical shifts because of their greater sensitivity to small differences in experimental parameters such as pH and ionic strength. The α-proton shifts for P43G and P43M agree well, except for positions 43−45 at the site of mutation and for Leu31. The α-proton of Leu31 is strongly shielded due to ring current effects from the solvent-exposed aromatic ring of Tyr13, which it packs directly against. Small changes in the relative orientation may result in large chemical shift changes for the α-proton of Leu31, as indicated by chemical shift calculations (Malmendal, A., and Gippert, G. P., unpublished). These data imply that the backbone structure remains unperturbed outside of the mutated regions.

The structural rearrangements occurring when P43G binds calcium are rather small (*23*), as compared to those occurring in the regulatory proteins such as skeletal troponin C (*24*−*26*) and calmodulin (*27*−*29*). However, there is a marked difference in the structural response to ion binding between the two EF-hands in calbindin D_{9k}. Only very minor

[1] Abbreviations: 2EF, A14D+A15Δ+P20Δ+N21G+P43M mutant of recombinant bovine calbindin D_{9k}; CPMG, Carr−Purcell−Meiboom−Gill; loop I, the N-terminal calcium-binding loop of calbindin D_{9k}, Ala/Asp14−Glu27; loop II, the C-terminal calcium-binding loop, Asp54−Glu65; helix I, Glu4−Asp14/Ala15; helix II, Lys25−Glu35; helix III, Leu46−Asp54; helix IV, Phe63−Ile73; linker, Phe36−Thr45; NOE, nuclear Overhauser effect; P43G, P43G mutant of recombinant bovine calbindin D_{9k}; P43M, P43M mutant of recombinant bovine calbindin D_{9k}; R_1, longitudinal relaxation rate constant; R_2, transverse relaxation rate constant.

[2] The number within parentheses indicates the amino acid residue number in calbindin D_{9k}.

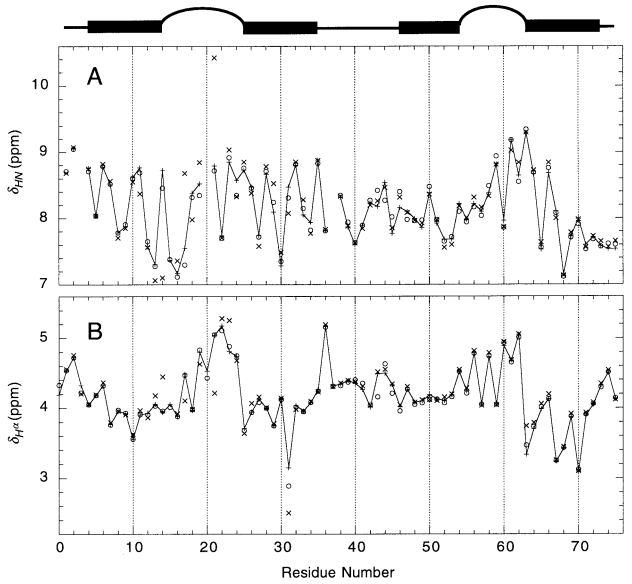

FIGURE 4: Comparison of amide (A) and α (B) proton chemical shifts for P43M (+, line) (*21*), P43G (○) (*72*), and 2EF (×). Dark rectangles represent α-helical regions, and arcs represent loop regions.

conformational changes are needed to accommodate the calcium ion in the N-terminal pseudo-EF-hand, while in the C-terminal regular EF-hand, the C-terminal end of helix III and the N-terminal end of helix IV move closer together and helix IV is extended from a purely α-helical conformation to a mixture of 3_{10}- and α-helix (*13, 14, 23*). In contrast to the small structural effects of ion binding, studies of ^{15}N spin relaxation of P43G (*30, 31*) and amide proton exchange of wild-type calbindin D_{9k} (*32*) and P43G (*33*) at different levels of calcium saturation reveal that calcium binding has dramatic effects on the dynamical properties of the protein on a wide range of time scales. The ^{15}N spin relaxation studies showed that the major effect of calcium binding is that the calcium-binding loops become less flexible on the picosecond to nanosecond time scale. Interestingly, this effect of ion binding is more pronounced in the shorter loop II than in the longer loop I. The relative rigidity of loop I was suggested to be due to the sequence characteristics of the pseudo-EF-hand loop, in particular the presence of a Pro (20) in the seventh position (*31*). Calcium binding also reduces the picosecond to nanosecond fluctuations of the most flexible helix, III. The important question of how the structural and dynamical properties of different types of EF-hands relate to their different functions has only recently been addressed (*23, 34*).

To further investigate the dependence of loop structure and dynamics on amino acid sequence and three-dimensional structural context, a calbindin D_{9k} mutant with loop I altered to a regular EF-hand loop was prepared (*22*). In this mutant, loop I is shortened by substituting the residue pair Ala14-Ala15 for a single Asp (14) and the residue pair Pro20-Asn21 for a single Gly (21) (see Figure 3); both the Asp in the first position and the Gly in the sixth positions are part of the consensus regular EF-hand sequence (*5*). The resulting mutant (A14D+A15Δ+P20Δ+N21G+P43M), henceforth referred to as 2EF, is constructed with a minimal number of residue substitutions, thereby minimizing possible perturbations of the surrounding helixes. As observed in the NMR solution structure (*22*), the backbone of loop I of the calcium-loaded form of 2EF adopts the conformation typical of a regular EF-hand loop, while there are no significant structural changes in the core of the protein. Calcium binding to 2EF is sequential with macroscopic binding constants $K_1 = 1.2 \times 10^8$ M^{-1} and $K_2 = 1.2 \times 10^7$ M^{-1} (*35*), but the cooperativity remains intact, as indicated by ^{113}Cd chemical shift changes during stepwise ion binding (*35*−*37*). The details of the calcium coordination and binding in 2EF are not of immediate concern to the present study, which focuses on the calcium-free (apo) state of 2EF.

Here, the backbone dynamics of apo-2EF are probed by ^{15}N spin relaxation measurements, which are sensitive mainly to picosecond to nanosecond conformational fluctuations. The results are compared to those of apo-P43G (*31*), thereby providing detailed information on the dependence of loop dynamics on sequence as well as on context. The former aspect is addressed by comparing the dynamics of a regular EF-hand loop and a pseudo-EF-hand loop, both anchored in a pseudo-EF-hand context (loop I of 2EF versus loop I of P43G); the latter aspect is addressed by the comparison of a regular EF-hand loop anchored in either a pseudo-EF-hand context or a regular EF-hand context (loop I of 2EF versus loop II of P43G or 2EF) and by the comparison of a regular EF-hand loop preceded by either a regular EF-hand loop neighbor or a pseudo-EF-hand loop neighbor (loop II of 2EF versus loop II of P43G). In addition, the comparison of the backbone dynamics of the linker segment in 2EF (which includes the P43M substitution) and P43G provides insights into the influence of the allowed backbone dihedral angle space on the local backbone flexibility.

MATERIALS AND METHODS

Protein Sample Preparation. Unlabeled and uniformly ^{15}N-labeled 2EF was expressed in *Escherichia coli* and purified as reported previously (*38*). Apoprotein (18 mg) was dissolved in 0.7 mL of 90% H_2O/10% D_2O, yielding a concentration of 3 mM. The pH was adjusted to 6.0 by microliter additions of 0.1 M HCl or NaOH. To eliminate dissolved oxygen, the ^{15}N-labeled sample was purged with argon before running the relaxation experiments.

NMR Spectroscopy. The spectra used for spin resonance assignments were recorded on a GE Omega 500 spectrometer at a ^{1}H frequency of 500.11 MHz. The assignments were obtained from COSY (*39*), R-COSY (30 ms mixing time) (*40*), 2Q (30 ms) (*41*), TOCSY (120 ms) (*42, 43*), and NOESY (200 ms) (*44*) experiments acquired on the unlabeled sample. HSQC-TOCSY (60 ms) and HSQC-NOESY (200 ms) (*45, 46*) experiments were acquired on the ^{15}N-labeled sample. The DIPSI-2 mixing sequence (*47*) was applied in both TOCSY experiments. The water signal was suppressed by low-power irradiation during the relaxation delay of 1.3 s, and the States method was used for frequency discrimination in ω_1 (*48*). All experiments were carried out at 300 K. ^{1}H chemical shifts were referenced to the water signal at 4.75 ppm, and the ^{15}N shifts were referenced indirectly to liquid NH_3 via the ^{1}H frequency of the water signal (*49, 50*).

The ^{15}N nuclear spin relaxation experiments were recorded at 499.84 (^{1}H) and 50.68 MHz (^{15}N) on a Varian Unity 500 spectrometer. ^{15}N spin−lattice (R_1) and spin−spin (R_2) relaxation rate constants, and steady-state {^{1}H}−^{15}N nuclear Overhauser effects (NOE) were measured using two-

dimensional proton-detected heteronuclear sensitivity-enhanced pulse sequences yielding two orthogonal data sets for each experiments. The pulse sequences were essentially identical with those used in the study of the P43G mutant (*31*). All spectra were recorded with a spectral width of 6410 Hz over 1024 complex points in ω_2 and the carrier frequency set on the H_2O signal. The water signal was suppressed by low-power presaturation during 1.3 s. The States-TPPI method was used for frequency discrimination in ω_1 (*51*). The spectral width in ω_1 was 1300 Hz, sampled over 64 complex t_1 points in the R_1 and R_2 experiments and 160 complex t_1 points in the NOE experiments; 8 transients were acquired per t_1 point in both the R_1 and R_2 experiments, and 32 transients were acquired in the NOE experiments. ^{15}N decoupling during acquisition was carried out using GARP-1 decoupling (*52*). GARP-1 was used for proton decoupling during the R_1 relaxation delays to suppress cross-correlation effects (*53*). The total relaxation delay between scans was 3.4 s in the R_1 and R_2 experiments and 4.8 s in the NOE experiment. The time interval between the refocusing pulses in the CPMG sequence (*54, 55*) used in the R_2 experiments was set to 1 ms to effectively eliminate the effects of evolution under the heteronuclear scalar coupling Hamiltonian (*56, 57*). The field strength of the ^{15}N refocusing pulses in the CPMG sequence was 3 kHz. Cross-correlation effects during the R_2 relaxation delay were suppressed by the application of ^1H 180° pulses synchronously with the even echoes in the CPMG sequence (*58, 59*). All measurements were carried out at a temperature of 300 K.

The R_1 values were obtained from 8 experiments with 7 different relaxation delays of 0.03 (×2), 0.11, 0.24, 0.48, 0.96, 1.50, and 2.94 s, and the R_2 values were obtained from 10 experiments with 7 different delays of 0.004 (×2), 0.030, 0.090, 0.180 (×2), 0.300, 0.700, and 1.300 s (×2). The duplicate experiments were used to evaluate the uncertainty in peak intensities. Four independent determinations of the heteronuclear NOE were made from two pairs of orthogonal data sets of two NOE experiments.

Data Processing and Analysis. Sequential assignments of ^1H and ^{15}N resonances were made following standard procedures (*60, 61*), using the in-house software MAGNE running on Sun Sparc 1 computers. The relaxation spectra were processed using the FELIX 3.0 software (Biosym Technologies, San Diego, CA) running on Iris Indigo 2 and Sun Sparc classic computers. A Lorentzian−Gaussian window function was applied in ω_2 and the data were zero-filled to 2048 points prior to Fourier transformation, followed by a second-order baseline correction. In the R_1 and R_2 experiments, the ω_1 interferograms were extended to 128 complex points using the linear prediction algorithm within FELIX 3.0. In all experiments, a Kaiser window function was used in ω_1. The final matrix size was 2048 × 512 real points after zero-filling and Fourier transformation. In the R_1 and R_2 experiments, the two orthogonal data sets were added to give a single data set with $\sqrt{2}$-increased signal-to-noise ratio, and in the NOE experiments the two orthogonal data sets were processed and analyzed separately.

Determination of ^{15}N Relaxation Parameters. The relaxation of a protonated ^{15}N nucleus spin is dominated by the dipolar interaction with the attached proton spin and the chemical shift anisotropy (CSA). The effects of these interactions are in turn dependent on the value of the spectral density function, $J(\omega)$, sampled at characteristic frequencies, resulting in the following expressions for the longitudinal (R_1) and transverse (R_2) relaxation rates and the heteronuclear NOE (*62*):

$$R_1 = (d^2/4)[J(\omega_H - \omega_N) + 3J(\omega_N) + 6J(\omega_H + \omega_N)] + c^2 J(\omega_N) \quad (1)$$

$$R_2 = (d^2/8)[4J(0) + J(\omega_H - \omega_N) + 3J(\omega_N) + 6J(\omega_H) + 6J(\omega_H + \omega_N)] + (c^2/6)[4J(0) + 3J(\omega_N)] + R_{ex} \quad (2)$$

$$\mathrm{NOE} = 1 + \frac{d^2}{4R_1}\frac{\gamma_H}{\gamma_N}[6J(\omega_H + \omega_N) - J(\omega_H - \omega_N)] \quad (3)$$

in which $d = \mu_0 h \gamma_H \gamma_N \langle 1/r_{HN}^3 \rangle / 8\pi^2$; $c = \omega_N \Delta\sigma / 3^{1/2}$; μ_0 is the permeability of free space; h is Planck's constant; γ_H and γ_N are the gyromagnetic ratios of ^1H and ^{15}N, respectively; $r_{HN} = 1.02$ Å is the N−H bond length; ω_H and ω_N are the Larmor frequencies of ^1H and ^{15}N, respectively; and $\Delta\sigma = -160$ ppm is the CSA. The expressions for R_2 include a chemical exchange term, R_{ex} (*63*).

The relaxation rate constants were obtained by nonlinear optimization (*64*) of the inversion−recovery and decay functions:

$$I(t) = I_\infty - [I_\infty - I_0] \exp(-R_1 t) \quad (4)$$

$$I(t) = I_0 \exp(-R_2 t) \quad (5)$$

where $I(t)$ is the intensity, measured as partial volumes of cross-peaks in the $^1H-^{15}N$ correlation spectra, at the relaxation delay t; I_0 is the intensity at $t = 0$; and I_∞ is the steady-state magnetization. The heteronuclear NOE was calculated as

$$\mathrm{NOE} = I_{sat}/I_{unsat} \quad (6)$$

where I_{sat} and I_{unsat} are the steady-state intensities measured with and without saturation of proton magnetization, respectively.

The apparent uncertainties in measured volumes were determined from duplicate spectra (*56*). In the R_1 and R_2 measurements, the uncertainties calculated for the shortest relaxation delays were used for all experiments. Uncertainties and goodness of fit of optimized parameters were evaluated as described in Palmer et al.[56] using Monte Carlo simulations of the distributions of peak volumes (*64*). The uncertainties in the NOE values were calculated from the four independent measurements by propagating the uncertainties of the intensities.

Model-Free Calculations. The relaxation data were interpreted using the extended model-free approach (*65*−*67*), in which the spectral density function is modeled as

$$J(\omega) = \frac{2}{5}\left[\frac{S^2\tau_m}{1 + (\omega\tau_m)^2} + \frac{(1 - S_f^2)\tau'_f}{1 + (\omega\tau'_f)^2} + \frac{(S_f^2 - S^2)\tau'_s}{1 + (\omega\tau'_s)^2}\right] \quad (7)$$

where $1/\tau'_f = 1/\tau_f + 1/\tau_m$; $1/\tau'_s = 1/\tau_s + 1/\tau_m$; τ_m is the overall rotational correlation time of the molecule; τ_f and τ_s are the effective correlation times for internal motions on the fast ($\tau_f < 100-200$ ps) and slow ($\tau_f < \tau_s < \tau_m$) time

scales, respectively; $S^2 = S_f^2 S_s^2$ is the square of the generalized order parameter characterizing the amplitude of internal motions; and S_f^2 and S_s^2 are the squares of the generalized order parameters for internal motions on the fast and slow time scales, respectively. S^2, S_f^2, and S_s^2 are henceforth referred to simply as "order parameters". Model-free parameters were selected using *F*-statistical testing (*68*). Briefly, this method involves optimizing five models, while keeping τ_m fixed to the value obtained from a trimmed R_2/R_1 ratio (*56, 69*):

Model 1. Motions on the slow time scale and chemical exchange are assumed negligible, and motions on the fast time scale are very fast ($\tau_f < 20$ ps). S_f^2 is optimized while the other parameters are kept fixed ($S_s^2 = 1$, $\tau_f = 0$, $R_{ex} = 0$).

Model 2. Motions on the slow time scale and chemical exchange are assumed negligible. S_f^2 and τ_f are optimized, ($S_s^2 = 1$, $R_{ex} = 0$).

Models 3 and 4. The same as models 1 and 2 but chemical exchange is not assumed negligible. S_f^2 and R_{ex} are optimized ($S_s^2 = 1$, $\tau_f = 0$); S_f^2, τ_f, and R_{ex} are optimized ($S_s^2 = 1$).

Model 5. Motions on the fast time scale are assumed very fast ($\tau_f < 20$ ps) and chemical exchange is negligible. S_f^2, S_s^2, and τ_s are optimized, ($\tau_f = 0$, $R_{ex} = 0$).

The model selection was performed using extensive Monte Carlo simulations to estimate the goodness of fit between dynamical models and the experimental data (*68*). For residues where the experimental data were within the 95% confidence limits of model 1, this model was selected. If the experimental data were not properly fit by model 1, but model 2 or 3 adequately represented the data, then these models were selected. Models 4 and 5 were used only if they could reproduce experimental data perfectly while none of the other models gave acceptable fits. For residues that were not properly fit using any model, *F*-statistics ($\alpha = 0.10$) were used to select either model 1, 2, or 3. In the final optimization, τ_m was included. Optimization and estimation of uncertainties in relaxation and model-free parameters were performed using the Model-Free 3.1 program package, kindly provided by Professor A. G. Palmer.

Rotational Diffusion Anisotropy. The degree of anisotropy was determined from the local diffusion constants, *D*, for each spin, as described previously (*70, 71*). Briefly, a set $\{D\}$ was obtained by fitting an isotropic diffusion model to the R_2/R_1 ratios for those bond vectors that experience only fast internal motion of low amplitude (i.e. τ_f and $1-S^2$ are small, and R_{ex} is less than 1.0 s^{-1} in the isotropic model-free optimization). For the case of an axially symmetric diffusion tensor of low anisotropy, *D* is given by (*70, 71*)

$$D = (D_{||} + D_{\perp})/2 + (D_{||} - D_{\perp})(x \sin\theta \cos\phi + y \sin\theta \sin\phi + z \cos\theta)^2/2 \quad (8)$$

in which $D_{||}$ and $D_{\perp}$ are the diffusion tensor elements parallel and orthogonal to the unique axis, respectively; *x*, *y*, *z* are the direction cosines of the N−H bond vector in a molecular frame; θ and ϕ are the angles that define the orientation of the symmetry axis of the diffusion tensor in the molecular frame. Equation 8 was solved by nonlinear least-squares optimization of the parameters $D_{\perp}$, θ, and ϕ against the experimental data pairs *D* and *x*, *y*, *z*, as described (*71*), using programs kindly provided by Professor A. G. Palmer. Because the structure of apo-2EF has not been determined, the atomic coordinates were taken from the ensemble of NMR structures of apo-P43G (*13*). Only residues located in the well-defined helixes were included in the optimization.

Statistical Analysis and Comparisons. The order parameters for the individual residues and structural elements were compared with the results for P43G (*31*). To minimize the possibility of a biased comparison, the order parameters for apo-P43G were recalculated from the original data using the same *F*-statistical selection method (*68*) described above. The individual comparisons were performed on the 95% confidence level. In the comparisons the structural elements were defined as follows: N-terminus (Met0−Pro3), helix I (Glu4−Asp14/Ala15), loop I (Lys16−Ser24), helix II (Lys25−Glu35), linker (Phe36−Thr45), helix III (Leu46−Asp54), loop II (Lys55−Ser62), helix IV (Phe63−Ile73) and C-terminus (Ser74−Gln75).

RESULTS AND DISCUSSION

Assignments. Complete ^{1}H and ^{15}N backbone resonance assignments of calcium-free 2EF were obtained. The assignments were facilitated by the close similarity of the chemical shifts to those of apo-P43G (*72, 73*). A comparison of the ^{1}H chemical shifts of apo-2EF with those of apo-P43G and apo-P43M is given in Figure 4. The observed differences between 2EF and P43M are mainly localized to the calcium-binding loops, while data for P43G also differ in the linker region, vide supra.

Relaxation Parameters. ^{15}N relaxation data for 2EF were analyzed for 64 out of 71 backbone N−H bond vectors. The amide proton of residue Lys1 could not be detected, presumably due to fast exchange with the solvent. Reliable relaxation parameters could not be calculated for Leu6/Asp19, Ile9/Leu39, and Ser62/Phe66 due to severe spectral overlap. The measured R_1 values are within the range 1.7−2.7 s^{-1}. When residues optimized using model 5 are omitted, the average value and standard deviation are 2.5 ± 0.2 s^{-1}. The average uncertainty in the R_1 values was estimated to be 1.1%. The R_2 values are within the range 3.1−7.7 s^{-1}. For residues without appreciable exchange contribution, the upper limit is 6.4 s^{-1}. When residues optimized using models 3−5 are omitted, the average value and standard deviation for R_2 are 5.7 ± 0.4 s^{-1}. The average uncertainty was initially estimated to 1.3%. The Monte Carlo simulations indicated that for 41 out of 64 residues either the peak volume uncertainties had been underestimated or the peak volumes did not decay as a single exponential. Because no statistical improvement was obtained when data were fit to biexponential functions, the decay functions were assumed to be singly exponential. When scaled to obtain an acceptable goodness of fit (*74*), the average uncertainty for R_2 increased to 2.5%. The NOE values are generally within the range 0.33−0.74. The lowest NOE value of 0.05 is observed for the C-terminal Gln75. If the residues optimized using model 5 are omitted, the average value and standard deviation are 0.66 ± 0.09. The average uncertainty in the NOE values was estimated to be 2.3%. The ranges of the experimental results are all in good agreement with those obtained for P43G (*31*).

Rotational Diffusion Anisotropy. Optimization of the axially symmetric diffusion model results in a mean value

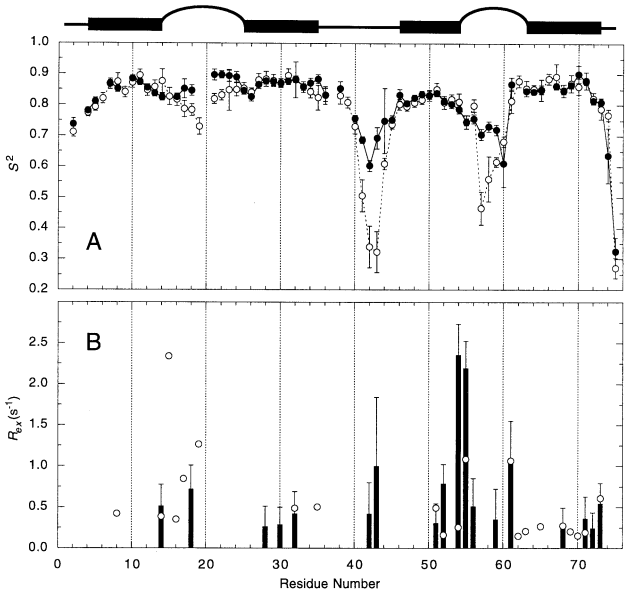

FIGURE 5: Model-free parameters for backbone N−H vectors of apo-2EF and -P43G as a function of residue number. (A) Order parameters (S^2) and (B) exchange terms (R_{ex}) for 2EF (●, filled bars) and P43G (○). The error bars represent the 95% confidence limits. Error bars for the P43G exchange terms are omitted to give a clearer view. Dark rectangles represent α-helical regions, and arcs represent loop regions.

$D_{||}/D_{\perp} = 1.05 \pm 0.01$, using the ensemble of 33 apo-P43G NMR structures (*13*), in good agreement with results for calcium-loaded P43G ($D_{||}/D_{\perp} = 1.07 \pm 0.01$ (*71*)). In the present case the axially symmetric model does not provide a statistically significant improvement over the isotropic model; the mean *F*-statistic of the ensemble is 0.88 and the *p*-value is 0.46. Thus, the values of the order parameters obtained herein by assuming isotropic rotational diffusion are accurate to within the limits of uncertainty, as discussed previously (*75*). However, the small degree of anisotropy observed indicates that residues with N−H vectors oriented along the unique axis of the diffusion tensor may have values of R_2 increased by ~2% over the result for isotropic rotational diffusion. The model-free protocol assuming isotropic diffusion may introduce artifactual R_{ex} terms for these residues to compensate for the effect of anisotropic diffusion. Thus, a conservative analysis indicates that only values of $R_{ex} > 0.3$ s^{-1} (on the 95% confidence level) are reliable indicators of conformational exchange.

Model-Free Parameters. The isotropic rotational correlation time, τ_m, calculated from the mean R_2/R_1 ratio is 4.21 ns. The final optimized value for τ_m was 4.12 ± 0.04 ns, compared to 4.14 ± 0.04 ns for P43G. The number of residues optimized using models 1−5 are 21, 17, 6, 12, and 3, respectively. The relaxation parameters for the remaining five residues (Glu5, Tyr13, Glu17, Gln22, Leu31) do not fit well to any model. Two of these residues were quantified using model 1, and the other three were quantified using model 2. Optimized order parameters are presented in Figure 5A.

With the new selection protocol, 23 out of 71 residues in P43G were quantified with a model different from the one used in (*31*). For 17 residues, the new model used a lower number of model-free parameters, while for 3 residues, a higher number was used. In 11 cases, model 1 replaced model 2. The only significant differences in order parameters were lower values for the five most flexible residues. These residues were quantified by using model 5 in both protocols.

Table 1: Average Order Parameters as a Function of Structural Element for Apo-2EF and -P43G at 300 K, pH 6.0[a]

structural element[b]	2EF	P43G
N-terminus	0.737 ± 0.018	0.712 ± 0.016
helix I	0.846 ± 0.001	0.847 ± 0.004
loop I	0.866 ± 0.002	0.810 ± 0.002
helix II	0.867 ± 0.001	0.864 ± 0.004
linker loop	0.741 ± 0.002	0.635 ± 0.002
helix III	0.819 ± 0.001	0.816 ± 0.003
loop II	0.734 ± 0.003	0.695 ± 0.002
helix IV	0.852 ± 0.001	0.855 ± 0.003
C-terminus	0.481 ± 0.023	0.520 ± 0.016

[a] The limits are 95% confidence limits of the mean value. [b] N-terminus, Met0−Pro3; helix I, Glu4−Asp14/Ala15; loop I, Lys16−Ser24; helix II, Lys25−Glu35; linker, Phe36−Thr45; helix III, Leu46−Asp54; loop II, Lys55−Ser62; helix IV, Phe63−Ile73; C-terminus, Ser74−Gln75. Note that, in the calculation of the averages, the first amino acid residue and the last three ones of each calcium-binding loop are included only in the helixes preceding and following the loop, respectively.

General Comparison to P43G. As shown in Figure 5A and Table 1, there is excellent agreement between P43G and 2EF in the values of the order parameters for the helical regions, attesting to a high reproducibility in the relaxation measurements. As mentioned previously the helixes are not inherently insensitive to perturbations in the loop regions, e.g., ion binding (*31*). The present results show that in the fast time regime probed here the modifications made to loop I and the linker region do not significantly affect the dynamical characteristics of the helical core region of the protein. In contrast, the altered sequence of loop I drastically affects the backbone fluctuations of both loop regions. In calcium-free P43G, the order parameters for the two calcium-binding loops are considerably lower than for the surrounding helixes, with lower values in the 12-residue C-terminal loop II than the 14-residue N-terminal loop I. In 2EF, the order parameters in both calcium-binding loops are significantly higher than for P43G. The observed reduction in flexibility of loop I deviates from the previous notion that a regular EF-hand calcium-binding loop is more flexible than a pseudo-EF-hand loop (*31*). The G43M substitution in the linker connecting the two EF-hands give rise to the largest local increase in order parameters with a mean of $\Delta S^2 > 0.1$. A pairwise comparison of order parameters for individual residues reveals significant differences for 23 positions, presented in Table 2. The order parameters are significantly higher in 2EF for residues Glu17, Gly18, Gly21, Gln22, and Ser24 in loop I (Figure 6A), and Gly57, Asp58, Gly59, and Val61 in loop II (Figure 7A). Significantly lower order parameters for Glu11, Asp14 at the end of helix I, and Asn56 in the beginning of loop II indicate that the helix−loop junctions are affected slightly by the substitutions in loop I. Order parameters are significantly higher for residues Lys41, Gly42, Met43, and Ser44 in the linker, for Thr34 and Glu35 terminating helix II, and for Leu46 starting helix III. Near the N- and C-termini of the protein, order parameters for Ser2, Glu5, and Val70 are significantly increased and that of Ser74 is significantly decreased by the substitutions.

Table 2: Order Parameters That Are Significantly Different in Apo-2EF and -P43G[a]

residue	2EF	P43G
Ser2	0.737 ± 0.018	0.712 ± 0.016
Glu5	0.811 ± 0.012*	0.792 ± 0.013
Glu11	0.873 ± 0.010	0.895 ± 0.018
Asp/Ala14	0.825 ± 0.011	0.876 ± 0.029
Glu17	0.852 ± 0.031*	0.786 ± 0.027
Gly18	0.847 ± 0.017	0.784 ± 0.019
Gly/Asn21	0.897 ± 0.018	0.820 ± 0.016
Gln22	0.898 ± 0.012*	0.832 ± 0.017
Ser24	0.890 ± 0.017	0.850 ± 0.021
Thr34	0.871 ± 0.016	0.843 ± 0.020
Glu35	0.883 ± 0.015	0.824 ± 0.040
Lys41	0.687 ± 0.011	0.506 ± 0.051
Gly42	0.603 ± 0.018	0.340 ± 0.067
Met/Gly43	0.693 ± 0.034	0.323 ± 0.066
Ser44	0.749 ± 0.105	0.609 ± 0.019
Leu46	0.833 ± 0.019	0.802 ± 0.017
Asn56	0.756 ± 0.015	0.799 ± 0.020
Gly57	0.706 ± 0.018	0.465 ± 0.053
Asp58	0.731 ± 0.016	0.560 ± 0.073
Gly59	0.720 ± 0.017	0.616 ± 0.016
Val61	0.868 ± 0.021	0.814 ± 0.038
Val70	0.901 ± 0.028	0.861 ± 0.026
Ser74	0.637 ± 0.089	0.768 ± 0.018

[a] Order parameters optimized with a nonoptimal model are marked with an asterisk. The limits are 95% confidence limits.

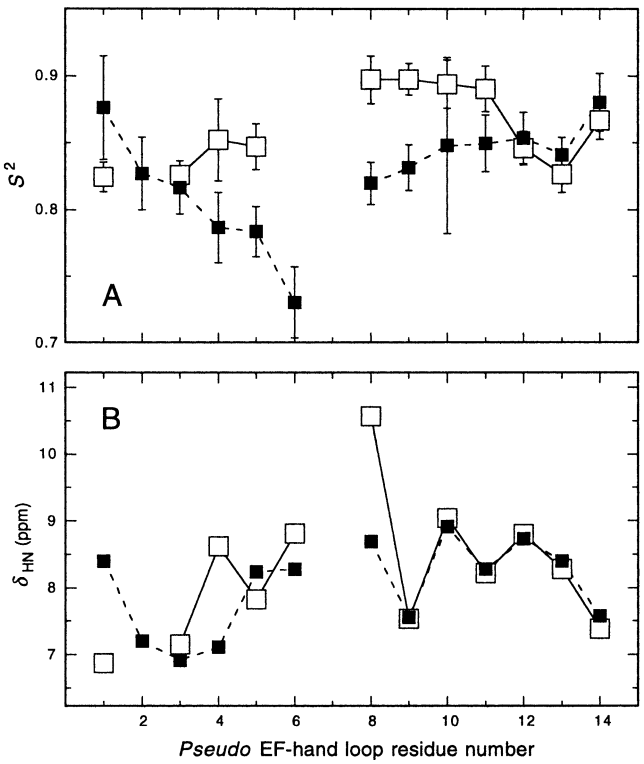

FIGURE 6: Order parameters and amide proton chemical shifts of regular EF-hand and pseudo-EF-hand loops in a pseudo-EF-hand context. (A) Order parameters for loop I in 2EF (□) and loop I in P43G (■), and (B) chemical shifts for loop I in 2EF (□) and loop I in P43G (■), as a function of pseudo-EF-hand loop position. The amino acid residues shown are for loop I in 2EF, Asp14, Δ, Lys16, Glu17, Gly18, Asp19, Δ, Gly21, Gln22, Leu23, Ser24, Lys25, Glu26, and Glu27; and loop I in P43G, Ala14, Ala15, Lys16, Glu17, Gly18, Asp19, Pro20, Asn21, Gln22, Leu23, Ser24, Lys25, Glu26, and Glu27. The error bars represent the 95% confidence limits and are in some cases smaller than the size of the symbol.

Loop Dynamics versus Linker Dynamics. The distant locations of these two regions (Figure 1), the localized

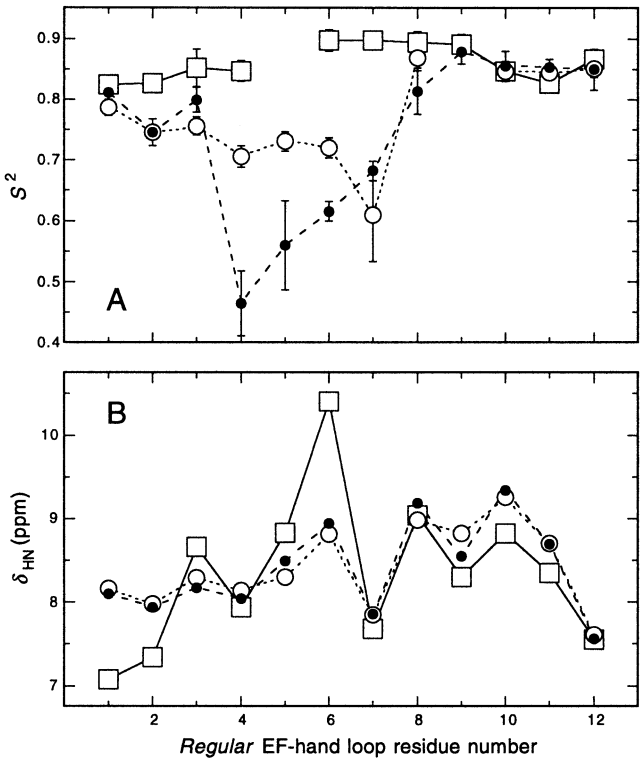

FIGURE 7: Order parameters and amide proton chemical shifts of residues in regular EF-hand loops in regular EF-hand and pseudo-EF-hand contexts. (A) Order parameters for loop I in 2EF (□), loop II in 2EF (○), and loop II in P43G (●), and (B) chemical shifts for loop I in 2EF (□), loop II in 2EF (○), and loop II in P43G (●), as a function of regular EF-hand loop position. The amino acid residues shown are for loop I in 2EF, Asp14, Lys16, Glu17, Gly18, Asp19, Gly21, Gln22, Leu23, Ser24, Lys25, Glu26, and Glu27; for loop II in 2EF and P43G, Asp54, Lys55, Asn56, Gly57, Asp58, Gly59, Glu60, Val61, Ser62, Phe63, Glu64, and Glu65; the error bars represent the 95% confidence limits and are in some cases smaller than the size of the symbol.

chemical shift differences induced by amino acid substitutions at the two sites of mutation (Figure 4), and the unperturbed dynamics of the helixes located between the two regions (Table 1 and Figure 5) indicate that the altered linker sequence has negligible effects on the picosecond to nanosecond dynamics of the calcium-binding loops and vice versa.

Effects of Loop Sequence in a Pseudo-EF-Hand Context. In the mutated, regular loop I of 2EF, the order parameters of Glu17−Ser24 (pseudo-EF-hand positions 4−11) are more than 0.04 unit higher than in the corresponding wild-type, pseudo-EF-hand loop I of P43G and of the same magnitude as in the surrounding helixes (Figures 5A and 6A). The major chemical shift differences between loop I of 2EF and loop I of P43G (Figure 6B) occur in the mutated region on the N-terminal side of the β-type interaction (positions 1−8). The downfield amide proton chemical shift of 10.42 ppm for the introduced Gly21 is correlated with the presence of a stabilizing hydrogen bond between Gly21 HN and Asp14 O^{δ} (*12*, *76*−*78*), vide infra. Negligible chemical shift differences in the C-terminal part of the loop (positions 9−14) indicate that the structure in this part of the loop is essentially unaffected by the mutations. Lower order parameters, as well as the upfield-shifted amide proton resonances of Glu11, Tyr13, and Ala/Asp14 ending helix I, suggest a slight disturbance of the structure and dynamics at the end of the helix. A slight rearrangement of the

aromatic ring of Tyr13 is indicated by changes in the chemical shifts of some protons located close to this ring, vide supra.

It has been shown previously that the modified loop I of 2EF folds into a regular EF-hand in the presence of calcium (*22*). The present results suggest that the regular EF-hand fold is very well accommodated by the pseudo-EF-hand context also when calcium is not bound. As compared with the pseudo-EF-hand sequence of P43G, the various substitutions in loop I in 2EF may be expected to have opposing effects on the dynamics; the shorter loop of 2EF is expected to decrease flexibility, whereas the substitution of a conformationally restricted Pro (20) for a less constrained Gly (21) is expected to increase flexibility. These data indicate that the former effect prevails over the latter. The contribution to the overall loop rigidity from the hydrogen bond formed between Gly21 and Asp14 may be significant in this respect.

Effects of Loop Context on a Regular EF-Hand Sequence. In the mutated loop I of 2EF, the order parameters of all loop residues in positions 1−9 are higher than for the corresponding residues in loop II of 2EF and P43G (Figure 7A). The different flexibility of loops I and II in 2EF indicates a strong dependence on the surrounding structure. Two possible sources for the higher flexibility of loop II are the less rigid "anchor" provided by helix III, as compared to the other helixes (Table 1), and the extended conformation of loop II observed in the apo state of P43G, with a distance between "anchoring points" in helixes III and IV that is long enough to severely disfavor the stabilizing Gly59 HN−Asp54 O^{δ} hydrogen bond. The hydrogen bond distance Gly59 HN−Asp54 $O^{\delta 2}$ is 3.1 ± 1.0 Å in apo-P43G compared to 2.2 ± 0.4 Å in the calcium-loaded state, and the distance between "anchoring points" Asp54 C^{α}−Phe63 C^{α} is 12.1± 1.0 and 10.5 ± 0.2 Å, respectively, (*13, 79*). In loop I, the corresponding distance Ala14 C^{α}−Lys25C^{α} is 10.4 ± 0.2 Å in both forms. The difference in population of this hydrogen bond and the analogous one in loop I is manifested by the amide proton chemical shift of 8.94 ppm for Gly59 compared to 10.42 ppm for Gly21. In the calcium-loaded form, the corresponding chemical shifts are 10.50 and 10.49 ppm (*22*), suggesting that the Gly21 HN−Asp14 O^{δ} hydrogen bond is highly populated in both forms, while the Gly59 HN−Asp54 O^{δ} hydrogen bond is formed only upon calcium binding.

The regulatory protein calmodulin consists of two independently folded regular EF-hand pair domains. There are strong stabilizing hydrogen bonds between the Asp and Gly residues in the equivalent positions in all four calcium-binding loops when calcium is bound (*80*). The apo structure of this protein (*28*) reveals that these hydrogen bonds in the N-terminal domain are rather independent of calcium binding, while there is a difference similar to what is observed for 2EF between the corresponding hydrogen bonds in the C-terminal domain; i.e., in this domain the hydrogen bond in "loop I" is formed without any bound calcium while it is absent in "loop II". The populations of the hydrogen bonds correlate well with the donor Gly amide proton chemical shifts (*76*). In the N-terminal domain of the closely related skeletal troponin C (*26, 81*), the corresponding stabilizing hydrogen bonds in both loops appear well formed regardless of calcium level, while in its C-terminal domain, chemical shifts indicate that both are significantly weakened by the absence of calcium (*82*). In calmodulin and troponin C, the domains in which these hydrogen bonds are not highly populated in the apo state also have the highest calcium affinity, suggesting a correlation between calcium affinity and the formation of this hydrogen bond (Malmendal, A., unpublished observation; ref *83*). Although this has not been shown for individual EF-hands, it might explain in part the lower affinity of site I in 2EF compared to wild-type calbindin D_{9k}.

The intact loop II in 2EF is more flexible than the modified loop I, but its flexibility is reduced compared to loop II in P43G, with substantial increases in the order parameters of Gly57, Asp58, and Gly59 (Figure 7A). This decrease in flexibility is explained by a damping effect of loop I, transmitted to loop II through the β-type interaction between residues Leu23 and Val61, both of which have increased order parameters in 2EF as compared to P43G. The unaltered amide proton chemical shift of Gly59 (Figure 7B) indicates that the reduced flexibility of 2EF loop II is not manifested in, or a result of, formation of the Gly59 HN−Asp54 O^{δ} hydrogen bond.

Conformational Exchange. Figure 5B shows the comparison of conformational exchange terms, R_{ex}, in 2EF and P43G. In 2EF, the residues that show the largest conformational exchange contributions to the transverse relaxation rates are Gly18, Glu52, Asp54, Lys55, and Val61, all of which are located in or near a calcium-binding site. The first two residues of loop II, Asp54 and Lys55, have high R_{ex} values (2.35 and 2.19 s^{-1} compared to 0.25 and 1.08 s^{-1} for P43G), indicating a difference in motions on the microsecond to millisecond time scale. Interestingly, R_{ex} for Val61 in the β-type interaction is not influenced by the mutations (R_{ex} = 1.03 s^{-1} in 2EF, compared to 1.06 s^{-1} in P43G). In P43G, the largest R_{ex} term, 2.34 s^{-1}, is found for Ala15 in the beginning of loop I, thus paralleling the exchange observed in the beginning of loop II of 2EF. The lower R_{ex} terms in loop I of 2EF indicate that motions on the microsecond to millisecond time scale get more constrained by the mutation, which may have consequences for the calcium-binding kinetics and equilibria. Because loop II in 2EF and both loops in P43G appear rather flexible in the calcium-free state, it is likely that the obtained values of R_{ex} truly reflect conformational exchange on a microsecond to millisecond time scale.

Effects of Substitutions in the Linker Region. The Met and Gly substitutions for the wild-type residue Pro43 in 2EF and P43G, respectively, affect the backbone order parameters in the linker region between the two EF-hands. Met is probably the more conservative substitution giving more wild-type-like dynamics. The lower number of allowed backbone conformations for the Gly42−Met43 sequence compared to Gly42−Gly43 (*84*) makes the backbone of the linker less flexible in 2EF than in P43G. In addition, any side-chain contacts of Met43 are expected to contribute to a reduced flexibility; however, the Met43 side chain does not pack tightly into the hydrophobic interior, and the linker appears flexible in the solution structure of calcium-loaded 2EF (*22*). The difference in order parameters is rather marked (Tables 1 and 2), including significantly higher values for linker residues Lys41, Gly42, Met43, and Ser44 of 2EF. The reduced flexibility also involves the immediately adjoining residues in the helixes bracketing the

linker (Thr34, Glu35, Leu46), but this effect does not permeate further into the core.

CONCLUDING REMARKS

The results presented here suggest that the structural and dynamical properties of the entire EF-hand, rather than the loop sequence per se, is the major determinant of loop flexibility in this system. The fact that the N-terminal EF-hand in P43G undergoes less structural and dynamical rearrangements upon calcium binding than the C-terminal site (*13*, *14*, *23*) cannot be explained simply as the effect of a more rigid loop structure arising as a consequence of the pseudo-EF-hand loop sequence. Instead, the entire pseudo-EF-hand appears to be built not to relax upon calcium release but to form a rigid structure that allows calcium binding with only minor rearrangements (*23*). The pseudo-EF-hand context of the regular EF-hand loop I in apo-2EF allows the loop to adopt a hydrogen-bonding pattern similar to that of the calcium-loaded state. The excellent agreement between order parameters in the helical regions and at the termini of P43G and 2EF demonstrates a high reproducibility in these measurements and further shows that the dynamics of the helical core region are quite independent of the structure and fast time scale dynamics of the intervening segments.

ACKNOWLEDGMENT

We thank Eva Thulin for protein expression and purification, Dr Anders L. Svensson for making available the crystal structure of calcium-loaded 2EF prior to publication, Johan Evenäs and Drs. Walter J. Chazin, Garry P. Gippert, Sara Linse, Arthur G. Palmer, III, and Anders L. Svensson for helpful discussions, and the Swedish NMR Center for usage of the Varian Unity 500 spectrometer.

SUPPORTING INFORMATION AVAILABLE

Tables of amide proton and nitrogen, and α-proton chemical shifts for 2EF, relaxation parameters (R_1, R_2, NOE) for 2EF, and model-free parameters (S^2, τ_s, R_{ex}) for 2EF and P43G, as a function of residue number (12 pages). Ordering information is given on any masthead page.

REFERENCES

1. Klee, C. B. (1988) in *Calmodulin* (Cohen, P., & Klee, C. B., Eds.) pp 35−56, Elseiver, New York.
2. Pochet, R., Lawson, P. E., and Heizman, C. W. (1990) *Calcium-binding proteins in normal and transformed cells*, Plenum Press, New York.
3. Whitfield, J. F. (1991) *Calcium, cell cycles and cancer*, CRC Press: Boca Raton, FL.
4. Kretsinger, R. H., and Nockolds, C. B. (1973) *J. Biol. Chem. 248*, 3313−3326.
5. Strynadka, N. C. J., and James, M. N. G. (1989) *Annu. Rev. Biochem. 58*, 951−998.
6. Falke, J. J., Drake, S. K., Hazard, A. L., and Peersen, O. P. (1994) *Q. Rev. Biophys. 27*, 219−290.
7. Kawasaki, H., and Kretsinger, R. H. (1994) *Protein Profile 1*.
8. Vogel, H. J., Drakenberg, T., Forsén, S., O'Neil, J. D. J., and Hofmann, T. (1985) *Biochemistry 24*, 3870−3876.
9. Schäfer, B. W., and Heizmann, C. W. (1996) *Trends Biochem. Sci. 21*, 134−40.
10. Christakos, S., Gabrielides, C., and Rhoten, W. B. (1989) *Endocr. Rev. 10*, 3−26.
11. Walters, J. R., Howard, A., Charpin, M. V., Gniecko, K. C., Brodin, P., Thulin, E., and Forsén, S. (1990) *Biochem. Biophys. Res. Commun. 170*, 603−608.
12. Kördel, J., Forsén, S., and Chazin, W. J. (1989) *Biochemistry 28*, 7065−7074.
13. Skelton, N. J., Kördel, J., and Chazin, W. J. (1995) *J. Mol. Biol. 249*, 441−462.
14. Akke, M., Forsén, S., and Chazin, W. J. (1995) *J. Mol. Biol. 252*, 102−121.
15. Szebenyi, D. M. E., and Moffat, K. (1986) *J. Biol. Chem. 261*, 8761.
16. Svensson, L. A., Thulin, E., and Forsén, S. (1992) *J. Mol. Biol. 223*, 601−606.
17. Andersson, M., Malmendal, A., Linse, S., Ivarsson, I., Forsén, S., and Svensson, L. A. (1997) *Protein Sci. 6*, 1139−1147.
18. Hofmann, T., Eng, S., Lilja, H., Drakenberg, T., Vogel, H. J., and Forsén, S. (1988) *Eur. J. Biochem. 172*, 307−313.
19. Chazin, W. E., Kördel, J., Drakenberg, T., Thulin, E., Brodin, P., Grundström, T., and Forsén, S. (1989) *Proc. Natl. Acad. Sci. U.S.A. 86*, 2195−2198.
20. Kördel, J., Forsén, S., Drakenberg, T., and Chazin, W. J. (1990) *Biochemistry 29*, 4400−4409.
21. Carlström, G., and Chazin, W. J. (1993) *J. Mol. Biol. 231*, 415−30.
22. Johansson, C., Ullner, M., and Drakenberg, T. (1993) *Biochemistry 32*, 8429−8438.
23. Skelton, N. J., Kördel, J., Akke, M., Forsén, S., and Chazin, W. J. (1994) *Nat. Struct. Biol. 1*, 239−245.
24. Herzberg, O., Mvult, J., and James, N. G. (1986) *J. Biol. Chem. 261*, 2638−2644.
25. Gagné, S. M., Tsuda, S., Li, M. X., Chandra, M., Smillie, L. B., and Sykes, B. D. (1994) *Protein Sci. 3*, 1961−1974.
26. Gagné, S. M., Tsuda, S., Li, M. X., Smillie, L. B., and Sykes, B. D. (1995) *Nat. Struct. Biol. 2*, 784−789.
27. Zhang, M., Tanaka, T., and Ikura, M. (1995) *Nat. Struct. Biol. 2*, 758−767.
28. Kuboniwa, H., Tjandra, N., Grzesiek, S., Ren, H., Klee, C. B., and Bax, A. (1995) *Nat. Struct. Biol. 2*, 768−776.
29. Finn, B. E., Evenäs, J., Drakenberg, T., Waltho, J. P., Thulin, E., and Forsén, S. (1995) *Nat. Struct. Biol. 2*, 777−783.
30. Kördel, J., Skelton, N. J., Akke, M., Palmer, A. G., and Chazin, W. J. (1992) *Biochemistry 31*, 4856−4866.
31. Akke, M., Skelton, N. J., Kördel, J., Palmer, A. G., and Chazin, W. J. (1993) *Biochemistry 32*, 9832−9844.
32. Linse, S., Teleman, O., and Drakenberg, T. (1990) *Biochemistry 29*, 5925−5934.
33. Skelton, N. J., Kördel, J., Akke, M., and Chazin, W. J. (1992) *J. Mol. Biol. 227*, 1100−1117.
34. Ikura, M. (1996) *Trends Biochem. Sci. 21*, 14−17.
35. Johansson, C., Brodin, P., Grundström, T., Forsén, S., and Drakenberg, T. (1991) *Eur. J. Biochem. 202*, 1283−1290.
36. Linse, S., Johansson, C., Brodin, P., Grundström, T., Drakenberg, T., and Forsén, S. (1991) *Biochemistry 30*, 154−162.
37. Linse, S., Bylsma, N. R., Drakenberg, T., Sellers, P., Forsén, S., and Thulin, E. (1994) *Biochemistry 33*, 12478−12486.
38. Johansson, C., Brodin, P., Grundström, T., Thulin, E., Forsén, S., and Drakenberg, T. (1990) *Eur. J. Biochem. 187*, 455−460.
39. Aue, W. P., Batholdi, E., and Ernst, R. R. (1976) *J. Chem. Phys. 64*, 2229−2246.
40. Wagner, G. (1983) *J. Magn. Reson. 55*, 151−156.
41. Braunschweiler, L., Bodenhausen, G., and Ernst, R. R. (1983) *Mol. Phys. 48*, 535−560.
42. Braunschweiler, L., and Ernst, R. R. (1983) *J. Magn. Reson. 53*, 521−528.
43. Bax, A. (1985) *J. Magn. Reson. 65*, 142−145.
44. Macura, S., and Ernst, R. R. (1980) *Mol. Phys. 41*, 95−117.
45. Bax, A., Ikura, M., Kay, L. E., Torchia, D. A., and Tschudin, R. (1990) *J. Magn. Reson. 86*, 304−318.
46. Norwood, T. J., Boyd, J., Heritage, J. E., Soffe, N., and Cambell, I. D. (1990) *J. Magn. Reson. 87*, 488−501.
47. Shaka, A. J., Lee, C. J., and Pines, A. (1988) *J. Magn. Reson. 77*, 274−293.

48. States, D. J., Haberkorn, R. A., and Ruben, D. J. (1982) *J. Magn. Reson. 48*, 286−292.
49. Bax, A., and Subramanian, S. J. (1985) *J. Magn. Reson. 67*, 565−569.
50. Live, D. H., Harris, D. G., Agosta, W. C., and Cowburn, D. (1984) *J. Am. Chem. Soc. 106*, 1939−1941.
51. Marion, D., Ikura, M., Tschudin, R., and Bax, A. (1989) *J. Magn. Reson. 85*, 393−399.
52. Shaka, A. J., Barker, P. B., and Freeman, R. (1985) *J. Magn. Reson. 64*, 547−552.
53. Boyd, J., Hommel, U., and Campbell, I. D. (1991) *Chem. Phys. Lett. 175*, 477−482.
54. Carr, H. Y., and Purcell, E. M. (1954) *Phys. Rev. 94*, 630−638.
55. Meiboom, S., and Gill, D. (1958) *Rev. Sci. Instrum. 29*, 688−691.
56. Palmer, A. G., Rance, M., and Wright, P. E. (1991) *J. Am. Chem. Soc. 113*, 4371−4380.
57. Skelton, N. J., Palmer, A. G., Akke, M., Kördel, J., Rance, M., and Chazin, W. J. (1993) *J. Magn. Reson. B102*, 253−264.
58. Palmer, A. G., Skelton, N. J., Chazin, W. J., Wright, P. E., and Rance, M. (1992) *Mol. Phys. 75*, 699−711.
59. Kay, L. E., Nicholson, L. K., Delaglio, F., Bax, A., and Torchia, D. A. (1992) *J. Magn. Reson. 97*, 359−375.
60. Chazin, W. J., and Wright, P. E. (1988) *J. Mol. Biol. 202*, 603−622.
61. Wüthrich, K. (1986) *NMR of Proteins and Nucleic Acids*, Wiley New York.
62. Abragam, A. (1961) *Principles of Nuclear Magnetism*, Clarendon Press, Oxford, U.K.
63. Bloom, M., Reeves, L. W., and Wells, E. J. (1965) *J. Chem. Phys. 42*, 1615−1624.
64. Press, W. H., Flannery, B. P., Teukolsky, S. A., and Vetterling, W. T. (1986) *Numerical recipes*, Cambridge University Press, Cambridge, U.K.
65. Clore, G. M., Szabo, A., Bax, A., Kay, L. E., Driscoll, P. C., and Gronenborn, A. M. (1990) *J. Am. Chem. Soc. 112*, 4989−4991.
66. Lipari, G., and Szabo, A. (1982) *J. Am. Chem. Soc. 104*, 4546−4559.
67. Lipari, G., and Szabo, A. (1982) *J. Am. Chem. Soc. 104*, 4559−4570.
68. Mandel, A. M., Akke, M., and Palmer, A. G. (1995) *J. Mol. Biol. 246*, 144−163.
69. Kay, L. E., Torchia, D. A., and Bax, A. (1989) *Biochemistry 28*, 8972−8979.
70. Brüschweiler, R., Liao, X., and Wright, P. E. (1995) *Science 268*, 886−889.
71. Lee, L. K., Rance, M., Chazin, W. J., and Palmer, A. G. (1997) *J. Biomol. NMR 9*, 287−298.
72. Skelton, N. J., Forsen, S., and Chazin, W. J. (1990) *Biochemistry 29*, 5752−5761.
73. Skelton, N. J., Akke, M., Kördel, J., Thulin, E., Forsén, S., and Chazin, W. J. (1992) *FEBS Lett. 303*, 136−40.
74. Stone, M. J., Fairbrother, W. J., Palmer, A. G., Reizer, J., Saier, M. H., and Wright, P. E. (1992) *Biochemistry 31*, 4394−4406.
75. Schurr, J. M., Babcock, H. P., and Fujimoto, B. S. (1994) *J. Magn. Reson. B105*, 211−224.
76. Ikura, M., Minowa, O., Yazawa, M., Yagi, K., and Hikachi, K. (1987) *FEBS Lett. 219*, 17−21.
77. Wishart, D. S., Sykes, B. D., and Richards, F. M. (1991) *J. Mol. Biol. 222*, 311−333.
78. Pardi, A., Wagner, G., and Wüthrich, K. (1983) *Eur. J. Biochem. 137*, 445−454.
79. Kördel, J., Skelton, N. J., Akke, M., and Chazin, W. J. (1993) *J. Mol. Biol. 231*, 711−734.
80. Chattopadhyaya, R., Meador, W. E., Means, A. R., and Quiocho, F. A. (1992) *J. Mol. Biol. 228*, 1177−1192.
81. Satyshur, K. A., Pyzalska, D., Greaser, M., Rao, S. T., and Sundaralingam, M. (1994) *Acta Crystallogr. D 50*, 40−49.
82. Tsuda, S., Hasegawa, Y., Yoshida, M., Yagi, K., and Hikichi, H. (1988) *Biochemistry 27*, 4120−4126.
83. Linse, S., and Forsén, S. (1995) in *Calcium Regulation of Cellular Function* (Means, A. R., Ed.) pp 89−152, Raven Press: New York.
84. Creighton, T. E. (1993) *Proteins, Structures and Molecular Properties*, 2nd ed., Freeman, New York.
85. Koradi, R., Billeter, M., and Wütrich, K. (1996) *J. Mol. Graphics 14*, 51−55.
86. Ferrin, T. E., Huang, C. C., Jarvis, L. E., and Langridge, R. (1988) *J. Mol. Graphics 6*, 13−27.

BI971798A